PAPER

Check for updates

An innovative synthesis of carbon-coated TiO₂ nanoparticles as a host for Na⁺ intercalation in sodium-ion batteries

Tanguy Soudant, [iD] Solenne Fleutot, Stéphanie Bruyère, Lucie Speyer, Sébastien Hupont, Mickaël Bolmont, Thomas Girardet, [iD] Loris Raspado, Claire Hérold and Sébastien Cahen [iD] *

In this work, an innovative route to synthesize an anatase TiO₂@C composite is presented. The synthesis was conducted using a soft chemistry microwave-assisted method using titanium(IV) butoxide as a titanium precursor. The residual (un)converted titanium precursor remaining after TiO₂ synthesis was used as a carbon precursor and thermally treated under H₂ to obtain nanoparticles of the TiO₂@C composite. A superior reversible specific capacity was obtained with TiO₂@C (120 mA h g⁻¹ at a C/20 rate, 3ʳᵈ cycle) compared to that with pristine TiO₂ (66.5 mA h g⁻¹ at a C/20 rate, 3ʳᵈ cycle), in agreement with the importance of carbon coating addition to TiO₂ nanoparticles as negative electrode materials for sodium-ion batteries.

Introduction

Currently, considering the environmental crisis, governments want to reduce greenhouse gas emissions. Therefore, electrification of the society is a way to free ourselves from the dependence on fossil fuels. The corresponding technological changes cause a very important demand for energy storage devices especially for electric vehicles (full electric or hybrid). Indeed, in 2016, the demand for batteries was around 41 GW h per year, which reached 550 GW h per year in 2022.[1] Nowadays, Li-ion batteries (LIBs) are widely used in mobile devices especially in electric vehicles thanks to their high energy density storage. Among the elements used for batteries, lithium, cobalt, nickel, copper and even carbon (graphite) will become critical elements in the medium term (2025–2035).[2] Moreover, lithium exploitation is not environmentally friendly, so it is necessary to develop sustainable alternatives for electrochemical storage technologies. Sodium-ion batteries (SIBs) appear as an interesting solution to free ourselves from the use of some critical elements cited previously. Unlike in LIBs, graphite cannot be used as a negative electrode material in SIBs due to poor sodium intercalation with a very low theoretical mass capacity of 35 mA h g⁻¹ for NaC₆₄ (372 mA h g⁻¹ for LiC₆).[3–5] Consequently, hard carbons remain the most widely studied anode materials because they are very good candidates for sodium ion storage. They present several advantages such

as the abundance of the carbon element, the low elaboration cost of hard carbons and their expected electrochemical performances (300 mA h g⁻¹) for an energy density of 300 W h kg⁻¹ for fully sodiated hard carbons.[6–8] Elsewhere, transition metal oxides are another possible class of anode materials and are considered for both LIBs and SIBs.[9–11] Among them, titanium dioxide (TiO₂) is an attractive alternative negative electrode material owing to the titanium abundance, its non-toxicity and cost-effectiveness. Such anodes could be envisaged in stationary application where high mass/volume capacities are not required. Another interesting feature of titanium dioxide compared with hard carbons is the safety aspect of TiO₂ as the nominal voltage of such an anode is 0.7 *versus* 0.1–0.05 V (*vs.* Na⁺/Na)[8], avoiding Na plating risks[12] with increased cyclability.[13] TiO₂ is a highly studied inorganic material due to its numerous applications in photocatalysis, cosmetics as a white pigment, optics, sensors and rechargeable batteries.[14] Many polymorphs of TiO₂ exist but the most common phases are rutile (tetragonal, $P4_2/mnm$), brookite (orthorhombic, *Pbca*) and anatase (tetragonal, $I4_1/amd$). The anatase polymorph is the most studied for applications in batteries due to its easy synthesis and electrochemical stability.[15–18] In particular, the anatase polymorph shows the highest sodium storage[13,19,20] as described in eqn (1), where y corresponds to the number of inserted Na⁺:

$$TiO_2 + yNa^+ + ye^- \leftrightarrow Na_yTiO_2 \qquad (1)$$
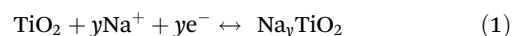
The nanoscale allows us to achieve better storage performance than the macroscale due to reduced diffusion lengths, a

Institut Jean Lamour, CNRS UMR 7198, Université de Lorraine, 54000 Nancy, France. E-mail: sebastien.cahen@univ-lorraine.fr

large specific surface area and high kinetic properties.[21–23] In the literature, Titanium NanoParticles (TNPs) are mostly synthesized by a hydrothermal route.[24,25] In this work, syntheses have been performed using a microwave-assisted procedure due to many advantages such as time gain, reduced power consumption, homogeneous heat and smaller sized particles obtained compared to the hydrothermal route.[26] Unfortunately, TNPs are electrochemically unstable toward electrolyte due to their huge specific surface area which causes an important irreversible consumption of Na^+ during the formation of the solid electrolyte interphase (SEI) at the electrode/electrolyte interface.[19,27] Therefore, many studies have been focused on the improvement of the electrochemical stability of TNPs. Indeed, when a three-dimensional TiO_2 anatase structure exhibits open galleries favourable for Na^+ insertion/deinsertion,[28] it suffers from low conductivity and slow ion diffusion.[29]

One cost-effective approach used for improving the capacity and rate capability is the formation of carbon coating surrounding TNPs. A porous carbon matrix will create preferential sites for Na^+ insertion/deinsertion, improving the contact between the active material and the electrolyte due to electrolyte penetration through pores and optimizing conduction paths for fast electron transport.[30,31]

It is expected that the carbon will add a synergetic effect, providing a conductive network that will also stabilize the SEI, improving the initial coulombic efficiency together with increased capacity and rate performances. Indeed, it has been demonstrated that the carbon coating allows improving the electronic conductivity of TNPs through the formation of a Ti–C bond, contributing to better electrochemical performances.[27,30] To coat nanoparticles, many routes exist such as sol–gel,[31,32] hydrothermal[33,34] or microwave-assisted[35] routes. In this work, we employed an one-pot TNP synthesis followed by direct thermal treatment without adding supplementary reactants. This original approach is assumed to improve the stability of TNPs by using $Ti(OCH_2CH_2CH_2CH_3)_4$ (TetraButOxyTitanium TBOT) as both titanium and carbon precursors. To do so, the as-prepared TNPs were thermally treated under H_2 flow.

Experimental

Synthesis of TiO₂@C nanoparticles

Usually, TiO_2 nanoparticles (TNPs) are mainly synthesized by the hydrothermal route.[24,25] In this work, all syntheses have been conducted using the microwave-assisted method which allows energy and time gains compared to the hydrothermal route.[26] To synthesize TNPs, samples were prepared in a glove bag under an argon atmosphere to prevent hydrolysis of TBOT. 4 mL of TBOT (Aldrich Chemical, 97%, CAS: 5593-70-4) and 8 mL of acetic acid (Sigma Aldrich, ≥99.8%, CAS: 64-19-7) were introduced into a microwave vial, then transferred into a single-mode microwave (Monowave 400 from Anton Paar) for thermal treatment at a temperature between 180 °C and 240 °C for 30 minutes and

finally cooling at 55 °C. The reaction mechanisms involved can be described by the following reactions:[36]

$$Ti(OBu)_4 + 4H_2O \rightarrow Ti(OH)_4 + 4BuOH \qquad (2)$$

$$Ti(OH)_4 \rightarrow TiO_2 + 2H_2O \qquad (3)$$
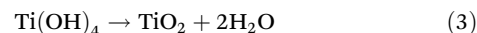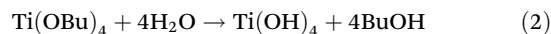
The obtained mixture containing TiO_2 nanoparticles was then washed once with absolute ethanol (VWR, 99.95%, CAS: 64-17-5) and twice with ultra-pure water (resistivity: 18.2 MΩ cm) by centrifugation for 5 minutes for each washing and then dried at 80 °C. The TNPs powder with the carbon precursor was loaded in a silica boat and thermally treated under H_2 flux (70 mL min⁻¹) for 4 h at 400 °C (5 °C min⁻¹) in a horizontal furnace.

Characterization

The TNPs phase was identified by powder X-ray diffraction (pXRD) using a Bruker diffractometer (D8 Advance) with Mo Kα radiation (0.70926 Å) in transmission mode and Cu Kα radiation (1.54060 Å) in reflection mode (θ–θ geometry). Thermogravimetric analyses (Setaram – Setsys EV1750) coupled with mass spectroscopy (Pfeiffer Vacuum – Omnistar GSD 301 C) were conducted at a heating rate of 5 °C min⁻¹ from room temperature to 800 °C and a cooling rate of 10 °C min⁻¹. Carbon in the samples was evidenced by Raman spectroscopy using a Horiba spectrometer (Labram HR800) operating at 457 nm wavelength. High-resolution transmission electron microscopy (HR-TEM) was performed (JEOL – ARM 200F) to study the morphology, size, and crystallinity of particles. Scanning TEM (STEM) mode was used for chemical analysis by electron energy loss spectroscopy (EELS).

Electrochemical characterization

To perform electrochemical characterization, a 70/10/20 slurry (70 wt% active material, 10 wt% carboxymethyl cellulose as a binder and 20 wt% carbon black as a conductive material) was prepared in deionized water and then coated on aluminium foil.[37] Once the slurry dried, the material was assembled on a current collector in coin cell CR2032 or in powder in a Swagelok® half-cell versus Na metallic foil with 1 M NaClO₄ in EC–DMC 1 : 1 in mass. Galvanostatic cycling with potential limitation (GCPL) tests were conducted on a Biologic – BCS-810 between 0 and 3 V vs. Na⁺/Na at a C/20 rate.

Results and discussion

Effect of the synthesis temperature

To study the temperature influence on the TNP crystallinity, four different synthesis temperatures were tested. In the XRD patterns shown in Fig. 1, the diffraction peaks can all be indexed to anatase TiO_2 only (COD no. 96-900-8216). The FWHM of the peaks decreases from 0.3149 to 0.2558 for 101 reflection and from 0.6298 to 0.3149 for the 200 reflection when the temperature increases, which characterizes a higher crystallite size (from 16 nm for 180 °C to 27 nm for 240 °C, cal-
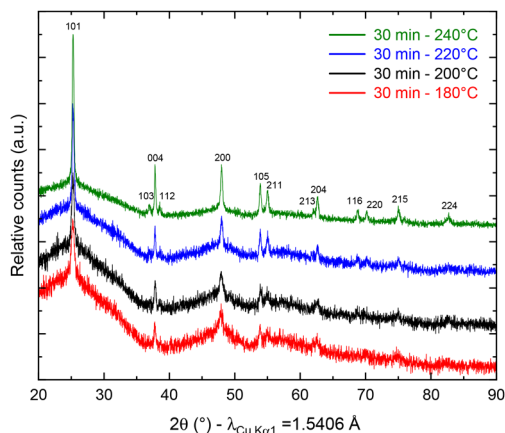
Fig. 1 pXRD patterns of anatase TiO_2 after synthesis at 180 (red), 200 (black), 220 (blue) and 240 °C (green).

culated using the Scherrer equation from the 101 peak). Moreover, a low angle background signal is detected due to the presence of residual amorphous material. This background decreases progressively upon increasing the temperature in agreement with the sharpening of the Bragg peaks accordingly to the higher crystallinity. Fig. 2 presents the ThermoGravimetric Analyses (TGA) of the sample synthesized at 180 °C. This thermogram is considered a representative of all samples of the study (data retrieved from other ones are summarized in Table 1). Such an analysis allows the quantification of the residual quantity of the titanium precursor after synthesis. Two mass loss signals are present: the first one is attributed to H_2O outgassing at 45 °C and the second one to the combustion of residual TBOT at 318 °C. Whatever the synthesis temperature was considered, the TBOT mass loss did not change, in agreement with a reaction yield close to 70%.

Thermal treatment

After synthesis, thermal treatment of TNPs under H_2-flux at 400 °C was carried out to remove TBOT residues and integrate
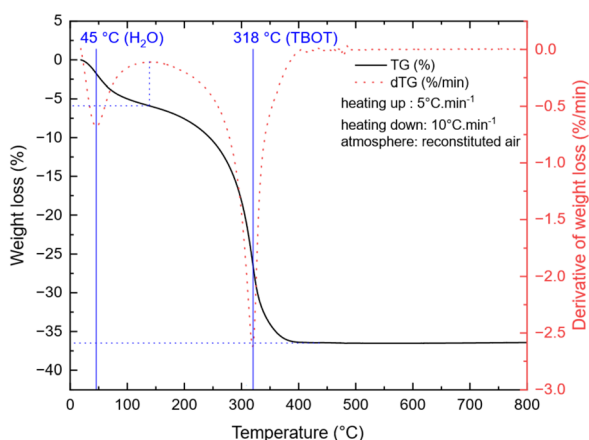
Table 1 Quantitative data of TG analysis at different synthesis temperatures

Synthesis temperature (°C)	H_2O weight loss (%)	Weight loss temperature (°C)	TBOT weight loss (%)	Decomposition temperature (°C)
180	6	45	31	318
200	7	43	30	317
220	6	42	30	318
240	4	54	27	314

TiO_2 into carbon. Indeed, residual TBOT present at around 30 wt% is assumed to be usable as a carbon precursor to form the carbon coating. pXRD patterns (Fig. 3) were recorded before and after thermal treatment under H_2 using a diffractometer with Mo $K_{\alpha1}$ radiation in order to probe the sample in transmission mode. pXRD patterns show no-TiO_2 reduction into Ti, as thermodynamically expected up to 500 °C. It should be noted that the TiO_2 polymorph is preserved, and the crystalline phase ratio is improved after thermal treatment. The SiO_2 reflection peak at 9.78°(2θ) is attributed to the silica boat used for the thermal treatment. Finally, the splitting of the peak around 11°(2θ) could be due to the 002 reflection of a poorly crystallized carbon. To confirm the presence of carbon after this step, TG-MS analysis was performed, and the results are presented in Fig. 4.

The weight loss can be decomposed into two phenomena as previously observed. The first one at around 45 °C is still attributed to H_2O outgassing, and the second one at around 370 °C (higher than for pristine TiO_2 nanoparticles) is correlated with CO_2 detected by mass spectroscopy. This second weight loss can be assigned to the combustion of around 3 wt% carbon. This carbon amount is in accordance with the amount reported by Devina *et al.* who obtained 0.2–4.1 wt%
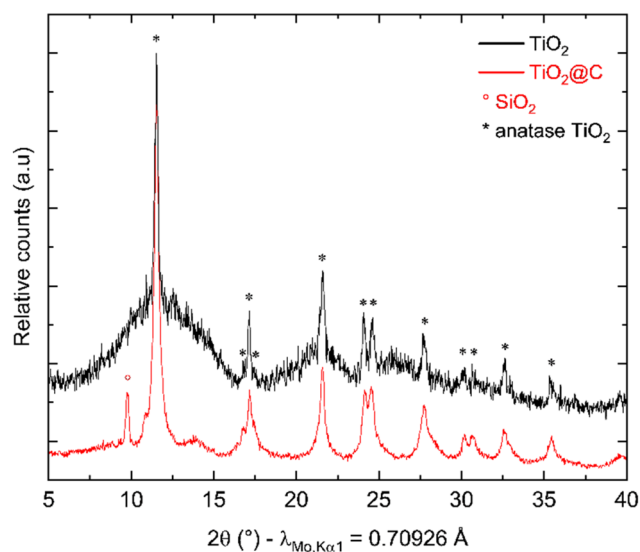

Fig. 2 TGA of TNPs after synthesis (180 °C, 30 min).

Fig. 3 pXRD patterns before (black) and after (red) heat treatment under H_2.
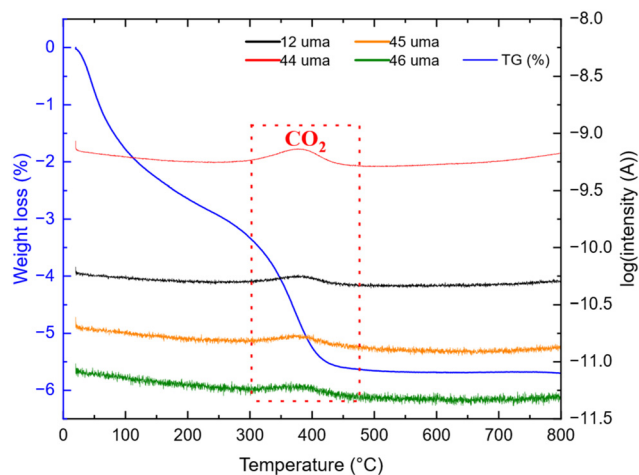
Fig. 4 TG-MS analysis of TNPs under air after thermal treatment.

microscopy (HR-TEM) was used to study the carbon morphology. Selected area electron diffraction (SAED) reveals the diffraction planes of anatase TiO_2 (Table 2) in accordance with the XRD measurement, and the good crystallinity of the par-

Table 2 Indexation from SAED

Yellow half-circle (#)	d-Spacing (nm)	(hkl)
(1)	0.3524	(101)
(2)	0.2394	(004)
(3)	0.1908	(200)
(4)	0.1711	(105)
(5)	0.1499	(213)

carbon depending on the carbon impregnation method.[38] The low combustion temperature is probably due to the amorphous nature of the carbon material formed on the surface of the particles.[39] Complementary to mass spectroscopy, Raman spectroscopy was performed to evidence the formation of carbon. Indeed, it is a powerful tool to characterize carbon materials. Six active Raman vibration modes due to the D_{2d} local symmetry of anatase TiO_2 are observed in the spectrum (Fig. 5): $1A_g + 2B_{1g} + 3E_g$ [40,41] in the range of 100–750 cm^{-1} is identified using a purple zone.

D and G bands present at 1376 and 1606 cm^{-1}, respectively, corroborate the presence of carbon materials as revealed after TGA analysis. The D band (disordered sp^2 carbon) is expected around 1350 cm^{-1} (ref. 31 and 42–45) but a shift is observed due to the excitation wavelength used.[46] Here, the I_D/I_G ratio is 0.22 but due to its parabolic evolution, it is not possible to conclude about carbon crystallinity. Indeed, as described by Merlen *et al.*, the D band intensity increases with disorder, reaches a maximum and then, decreases when carbon is close to amorphous.[47] High-resolution transmission electronic
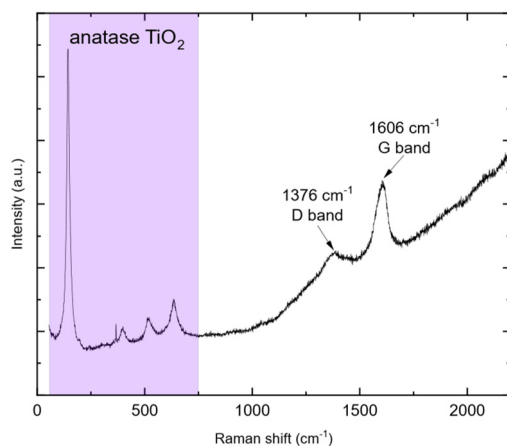

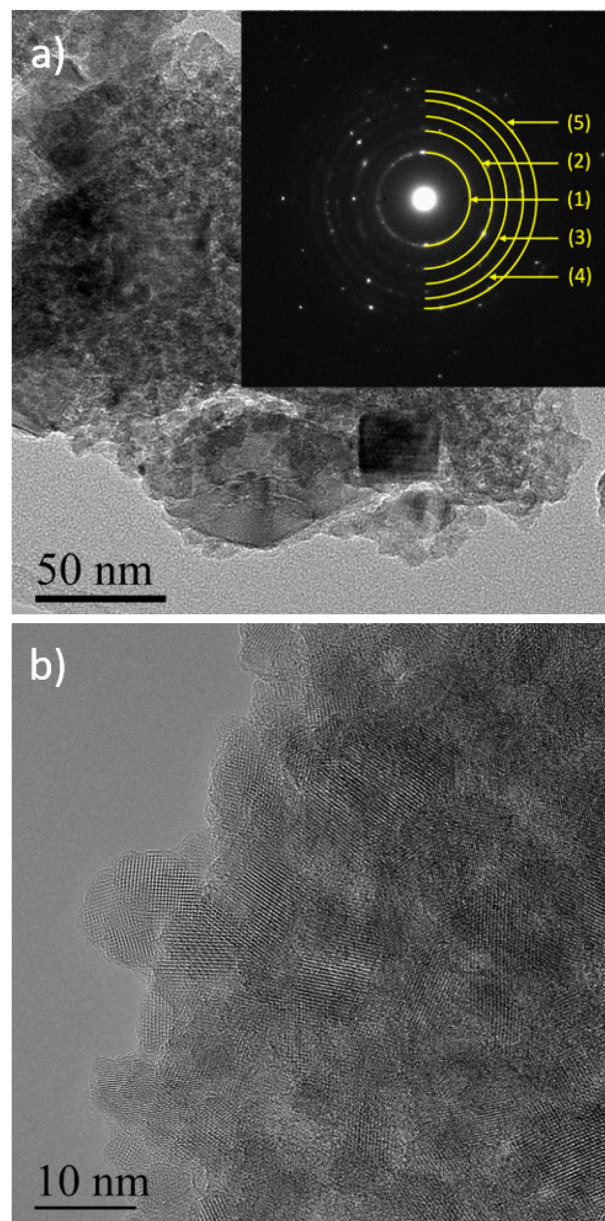
Fig. 5 Raman spectrum of TiO$_2$@C (457 nm wavelength).
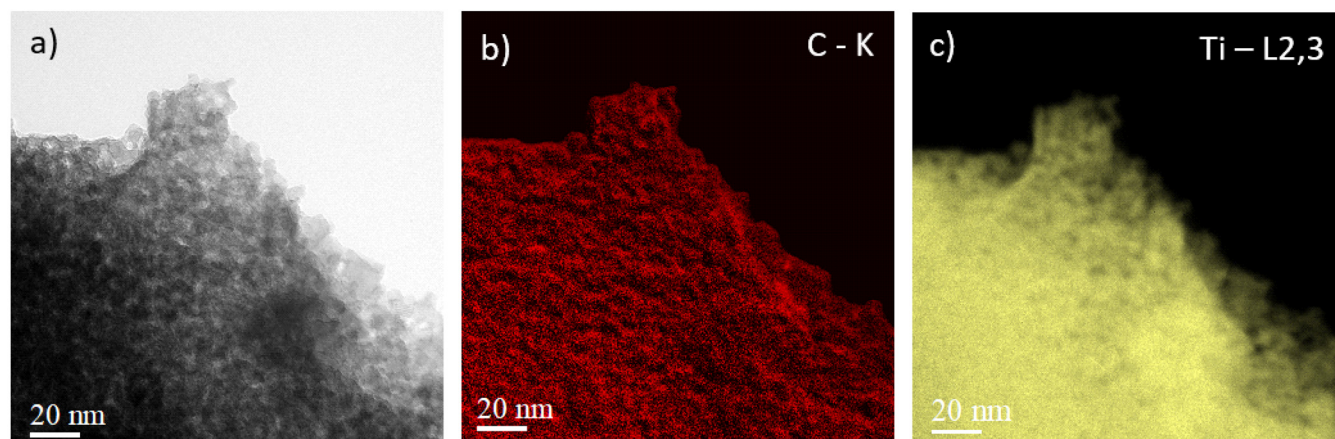

Fig. 6 BF-TEM with SAED (a) and HR-TEM of TiO$_2$@C (b).

Fig. 7 BF-TEM (a) and TEM elemental mapping images of carbon (b) and titanium (c) for $TiO_2@C$.

ticles. First, the TEM micrograph (Fig. 6(a)) exhibits particles aggregated into an amorphous matrix. The HR-TEM micrograph (Fig. 6(b)) evidences the atomic planes of the particles demonstrating the crystallinity of titanium dioxide and allows us to determine the size of the crystals, which is 8.5 ± 1.4 nm in accordance with XRD calculation. STEM-EDX elemental mapping images highlight the presence of carbon (Fig. 7). Thus, TG-MS, Raman spectroscopy and HR-TEM confirm the presence of carbon in samples thermally treated under H_2 using TBOT as a carbon precursor.

Electrochemical characterization

Pristine TiO_2. Galvanostatic curves of pristine TNPs (*i.e.*, without carbon) are presented in Fig. 8. On the first discharge (sodiation) curve, three slopes can be noted: the first one between 2 and 1.2 V *vs.* Na^+/Na, the second one between 1.2 and 0.25 V *vs.* Na^+/Na and the last one until 0 V *vs.* Na^+/Na. Wu *et al.* have described that the first one at high potential is related to a pseudo-capacitive process where no structural changes are observed.[13] Then, Na^+ insertion occurs with a

structural transition and finally a disproportionation reaction with intermediate phase formation. The next cycle curves adopt an S-shape due to poor low crystallinity. The first discharge curve indicates an intercalation of 0.75 Na^+ and a deintercalation of only 0.25 Na^+ into TiO_2 which corresponds to an irreversible capacity of 175 mA h g^{-1} and a reversible capacity of 75 mA h g^{-1}. A fraction of Na^+ ions are continuously consumed to form the SEI, as shown by the shift of curves to lower capacity values, especially after the first cycle. In the 20th cycle, 0.18 Na^+ can be intercalated and 0.17 Na^+ are deintercalated. These results demonstrate the electrochemical instability of TiO_2 nanoparticles towards the electrolyte (Fig. 8). The evolution of the capacity *versus* the number of cycles shows that the first irreversible capacity is significant, and the capacity continuously decreases (Fig. 9). In the first cycle, the columbic efficiency reaches 30% due to SEI formation and reaches 95% in the 20th cycle which is an acceptable value for this kind of material and corresponds to the results mentioned by Ge *et al.*[27] Specific capacity goes down to 60 mA h g^{-1} in the
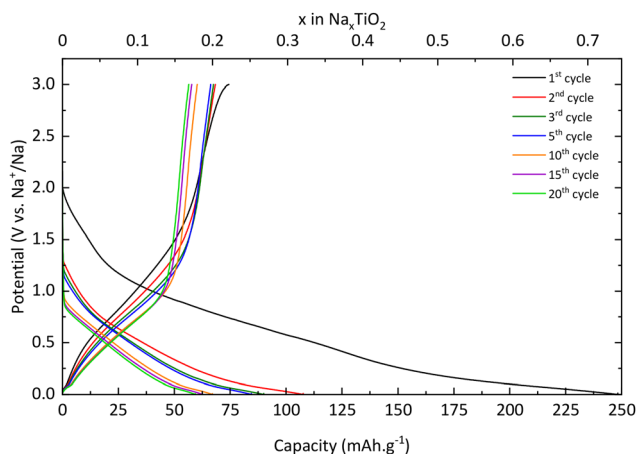

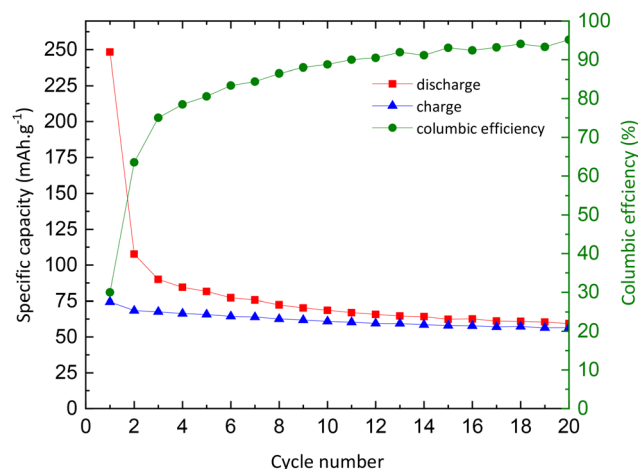**Fig. 8** Charge/discharge curves of pristine TiO_2 at a C/20 rate.

Fig. 9 Evolution of charge (blue) and discharge (red) capacities, and columbic efficiency (green) as a function of the number of cycles.
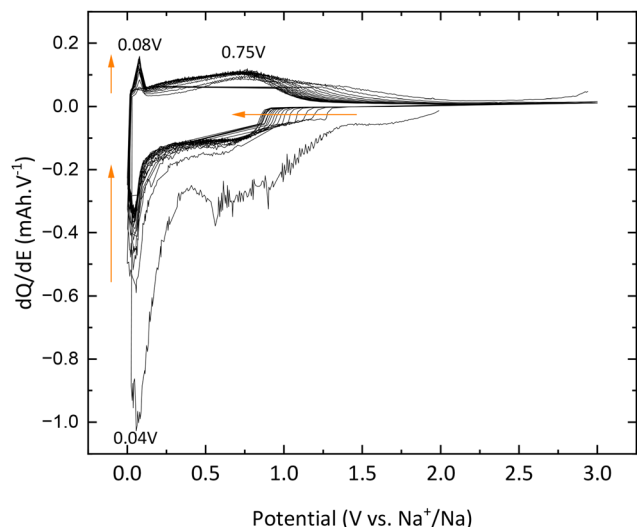
Fig. 10   dQ/dE curves of pristine TiO_2.

Fig. 11   Charge/discharge curves of TiO_2@C.

20th cycle, below the values mentioned in the literature.[11,13,19,27,37] 30% TBOT residues after the synthesis as the electronic insulator can explain this result. Incremental dQ/dE versus E curves presented in Fig. 10 allow the determination of the sodiation reaction potentials. In the reduction path, the two peaks at 0.04 and 0.75 V vs. Na^+/Na correspond to the sodiation reaction (eqn (4)):

$$xNa^+ + xe^- + TiO_2 \rightarrow Na_xTiO_2 \qquad (4)$$
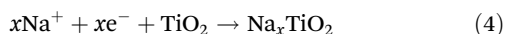
The desodiation reaction takes place at the same potential as the sodiation reaction i.e., 0.75 V vs. Na^+/Na (eqn (5)):

$$Na_xTiO_2 \rightarrow xNa^+ + xe^- + TiO_2 \qquad (5)$$
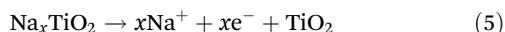
In addition, the peaks at 0.04 V vs. Na^+/Na in reduction and 0.08 V vs. Na^+/Na are also attributed to electrolyte decomposition according to Wu et al.[13] Finally, the signal between 1.3 and 0.9 V vs. Na^+/Na, which shifts to lower and lower potential values, is due to SEI formation, which corroborates the results previously mentioned and demonstrates the electrochemical instability of TNPs toward the electrolyte.

TiO$_2$@C. TNPs with carbon (TiO$_2$@C) were prepared as described in the Experimental section. As for pristine TiO$_2$, galvanostatic measurements were used to characterize the electrochemical properties of TNPs@C. In Fig. 11, the first discharge curve reveals a capacity of 220 mA h g^{-1} which corresponds to 0.65 intercalated Na^+, with a very long plateau at low potential and during the first charge, 0.33 Na^+ are deintercalated. In the 3rd cycle, the capacity reaches 115 mA h g^{-1}, twice that of pristine TiO$_2$. Then, the capacity in the 20th cycle reaches 76 mA h g^{-1} (retention capacity of 67%), which is much higher than that of pristine TiO$_2$. Different values are summarized in Table 3. SEI formation seems to be reduced, demonstrating the stabilization of TNPs embedded in carbon compared to pristine TiO$_2$. Indeed, the initial coulombic efficiency in the 1st cycle is 51% versus 30% for pristine TiO$_2$.
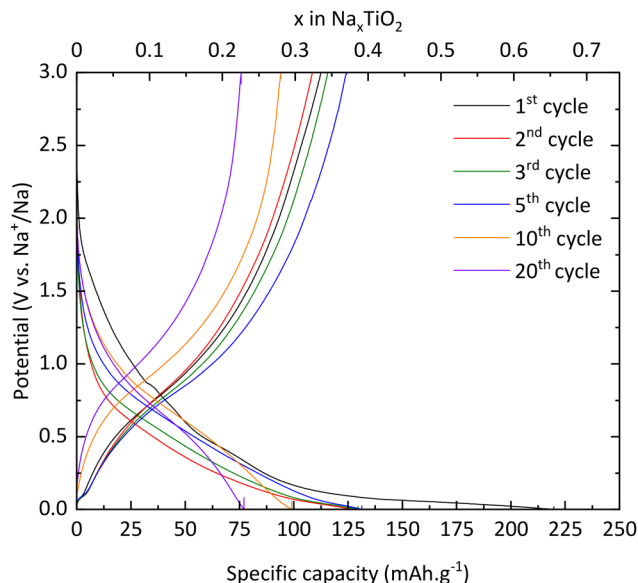
Table 3   Summary of characteristic values

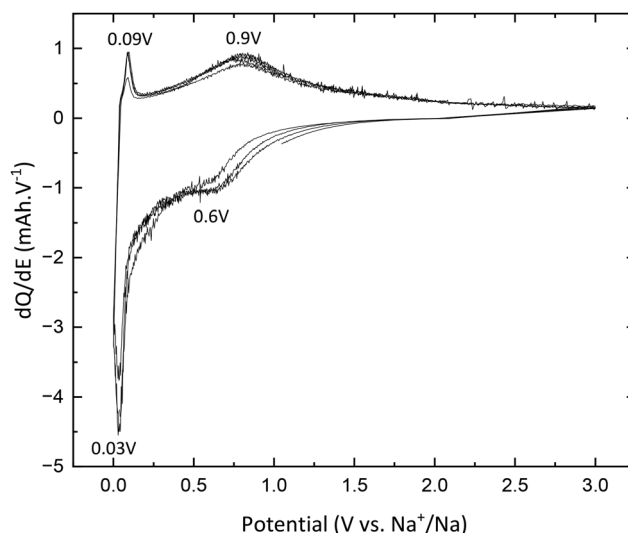|	Q discharge (mA h g^{-1}) – x_{Na}	Q charge (mA h g^{-1}) – x_{Na}	Efficiency (%)
Pristine TiO$_2$			
Cycle 1	248.3–0.74	74.1–0.22	30
Cycle 3	90–0.27	67.5–0.20	75
Cycle 5	81.6–0.24	65.8–0.20	80.6
Cycle 10	68.6–0.20	60.9–0.18	88.8
Cycle 20	59.3–0.18	56.5–0.17	95.2
TiO$_2$@C			
Cycle 1	219.8–0.65	112.6–0.34	51.2
Cycle 3	129.5–0.39	115.7–0.34	89.3
Cycle 5	131.3–0.39	124.2–0.37	94.6
Cycle 10	128.7–0.38	128.2–0.38	99.6
Cycle 20	77.1–0.23	75.7–0.22	98.2

Fig. 12   dQ/dE curves of TiO@C.

Therefore, the carbon contribution to the stabilization and the improvement of electrochemical performances is significant. The dQ/dE curve presented in Fig. 12 shows that sodium deinsertion (eqn (4)) takes place at a higher potential *i.e.*, 0.9 V *vs.* Na^+/Na than for pristine TiO_2 and the insertion mechanism (eqn (5)) occurs at 0.6 V *vs.* Na^+/Na which corresponds to the one mentioned by Ge *et al.*[27] Moreover, electrolyte decomposition and sodium redox reactions still happen at low potentials.

Conclusions

Titanium dioxide nanoparticles were successfully obtained by the microwave-assisted method. TBOT residues were used as a carbon precursor to prepare carbon-embedded TNPs. TNPs@C exhibits electrochemical stabilization by improving the efficiency during the first cycle which corresponds to a decrease in the SEI formation. Upon carbon addition, the capacity reached 115 mA h g^{-1} in the 3rd cycle against the 67 mA h g^{-1} for pristine TNPs. The electrochemical performances of TiO_2@C presented in this work are still lower than those mentioned in other studies.[11,31,48] Even though our results are promising, with an ICE of only 51% and a capacity retention of 67%, the materials need further optimization (size and shape of TiO_2 nanoparticles; anchorage, thickness and porosity of the carbon matrix) before widespread commercialisation. The goal of this work is not the full optimization of the electrochemical performances and cycle life of TiO_2 as an anode for sodium-ion batteries, but mainly to provide a proof-of-concept for the innovative and simple synthesis of TiO_2@C intercalation materials. Here, this work presents an original way for synthesizing TiO_2 nanoparticles by a fast microwave-assisted route. Moreover, it constitutes an advanced demonstration of the possibility of using one precursor as both Ti and C precursors. Nevertheless, the optimization of the TiO_2@C material can be considered on several points: control of the residual amorphous material after the microwave-assisted step, morphology and crystallinity of TiO_2 anatase, carbon matrix optimization, *etc.*

Moreover, the electrochemical stabilization of TiO_2 nanoparticles toward the electrolyte was proved thanks to carbon addition.

Author contributions

Tanguy Soudant: formal analysis, investigation, writing – original draft, writing – review & editing, and visualization. Solenne Fleutot: conceptualization, methodology, validation, investigation, review & editing, visualization, and supervision. Stephanie Bruyère: formal analysis and review & editing. Lucie Speyer: formal analysis and review & editing. Mickaël Bolmont: methodology and review & editing. Thomas Girardet: methodology and review & editing. Loris Raspasdo: methodology and review & editing. Claire Hérold: conceptualization, writing – review & editing, and visualization. Sébastien Cahen: conceptualization, methodology, validation, formal analysis, resources, writing – review & editing, visualization, funding acquisition, supervision, and project administration.

Conflicts of interest

There are no conflicts to declare.

Acknowledgements

References

1 Battery demand by region, 2016–2022 – Charts – Data & Statistics, **https://www.iea.org/data-and-statistics/charts/battery-demand-by-region-2016-2022**, (accessed January 24, 2024).

2 H. Kim, *ACS Mater. Au*, 2023, **3**, 571–575.

3 D. A. Stevens and J. R. Dahn, *J. Electrochem. Soc.*, 2001, **148**, A803.

4 M. M. Doeff, Y. Ma, S. J. Visco and L. C. D. Jonghe, *J. Electrochem. Soc.*, 1993, **140**, L169.

5 P. Ge and M. Fouletier, *Solid State Ion.*, 1988, **28–30**, 1172–1175.

6 V. Palomares, P. Serras, I. Villaluenga, K. B. Hueso, J. Carretero-González and T. Rojo, *Energy Environ. Sci.*, 2012, **5**, 5884.

7 S. Tan, H. Yang, Z. Zhang, X. Xu, Y. Xu, J. Zhou, X. Zhou, Z. Pan, X. Rao, Y. Gu, Z. Wang, Y. Wu, X. Liu and Y. Zhang, *Molecules*, 2023, **28**, 3134.

8 W. Lu, Z. Wang and S. Zhong, *J. Phys.: Conf. Ser.*, 2021, **2109**, 012004.

9 H. Pan, Y.-S. Hu and L. Chen, *Energy Environ. Sci.*, 2013, **6**, 2338–2360.

10 S.-W. Kim, D.-H. Seo, X. Ma, G. Ceder and K. Kang, *Adv. Energy Mater.*, 2012, **2**, 710–721.

11 Y. Xu, E. M. Lotfabad, H. Wang, B. Farbod, Z. Xu, A. Kohandehghan and D. Mitlin, *Chem. Commun.*, 2013, **49**, 8973.

12 D. Aurbach, *Solid State Ionics*, 2002, **148**, 405–416.

13 L. Wu, D. Bresser, D. Buchholz, G. A. Giffin, C. R. Castro, A. Ochel and S. Passerini, *Adv. Energy Mater.*, 2015, **5**, 1401142.

14 U. Diebold, *Surf. Sci. Rep.*, 2003, **48**, 53–229.

15 D. Deng, M. G. Kim, J. Y. Lee and J. Cho, *Energy Environ. Sci.*, 2009, **2**, 818.

16 S. Liang, X. Wang, Y.-J. Cheng, Y. Xia and P. Müller-Buschbaum, *Energy Storage Mater.*, 2022, **45**, 201–264.

17 O. Eroglu and H. Kizil, *J. Phys. Chem. Solids*, 2023, **178**, 111352.

18 Y.-X. Wu, S.-F. Liu, R. Lu, C. Liu and Q. Sun, *Ionics*, 2023, **29**, 2723–2733.

19 W. Wang, Y. Liu, X. Wu, J. Wang, L. Fu, Y. Zhu, Y. Wu and X. Liu, *Adv. Mater. Technol.*, 2018, **3**, 1800004.

20 J. Patra, S.-C. Wu, I.-C. Leu, C.-C. Yang, R. S. Dhaka, S. Okada, H.-L. Yeh, C.-M. Hsieh, B. K. Chang and J.-K. Chang, *ACS Appl. Energy Mater.*, 2021, **4**, 5738–5746.

21 J. Jamnik and J. Maier, *Chem. Phys.*, 2003, **5**, 5215.

22 K. T. Lee and J. Cho, *Nano Today*, 2011, **6**, 28–41.

23 J.-Y. Shin, D. Samuelis and J. Maier, *Adv. Funct. Mater.*, 2011, **21**, 3464–3472.

24 S. Y. Chae, M. K. Park, S. K. Lee, T. Y. Kim, S. K. Kim and W. I. Lee, *Chem. Mater.*, 2003, **15**, 3326–3331.

25 H.-G. Jung, S. W. Oh, J. Ce, N. Jayaprakash and Y.-K. Sun, *Electrochem. Commun.*, 2009, **11**, 756–759.

26 F. Dufour, S. Cassaignon, O. Durupthy, C. Colbeau–Justin and C. Chanéac, *Eur. J. Inorg. Chem.*, 2012, **2012**, 2707–2715.

27 Y. Ge, H. Jiang, J. Zhu, Y. Lu, C. Chen, Y. Hu, Y. Qiu and X. Zhang, *Electrochim. Acta*, 2015, **157**, 142–148.

28 D. Su, S. Dou and G. Wang, *Chem. Mater.*, 2015, **27**, 6022–6029.

29 Y. Yang, X. Ji, M. Jing, H. Hou, Y. Zhu, L. Fang, X. Yang, Q. Chen and C. E. Banks, *J. Mater. Chem. A*, 2015, **3**, 5648–5655.

30 X. Ma, Z. Zhang, J. Tian, B. Xu, Q. Ping and B. Wang, *Funct. Mater. Lett.*, 2018, **11**, 1850021.

31 H. Tao, M. Zhou, K. Wang, S. Cheng and K. Jiang, *Sci. Rep.*, 2017, **7**, 43895.

32 A. C. Martins, A. L. Cazetta, O. Pezoti, J. R. B. Souza, T. Zhang, E. J. Pilau, T. Asefa and V. C. Almeida, *Ceram. Int.*, 2017, **43**, 4411–4418.

33 K. Olurode, G. M. Neelgund, A. Oki and Z. Luo, *Spectrochim. Acta, Part A*, 2012, **89**, 333–336.

34 M. Maletić, M. Vukčević, A. Kalijadis, I. Janković-Častvan, A. Dapčević, Z. Laušević and M. Laušević, *Arabian J. Chem.*, 2019, **12**, 4388–4397.

35 C. Coromelci-Pastravanu, M. Ignat, E. Popovici and V. Harabagiu, *J. Hazard. Mater.*, 2014, **278**, 382–390.

36 M. J. Velasco, F. Rubio, J. Rubio and J. L. Oteo, *Spectrosc. Lett.*, 1999, **32**, 289–304.

37 L. Wu, D. Buchholz, D. Bresser, L. Gomes Chagas and S. Passerini, *J. Power Sources*, 2014, **251**, 379–385.

38 W. Devina, D. Nam, J. Hwang, C. Chandra, W. Chang and J. Kim, *Electrochim. Acta*, 2019, **321**, 134639.

39 K. Judai, N. Iguchi and Y. Hatakeyama, *J. Chem.*, 2016, **2016**, 1–6.

40 K. Gao, *Phys. B*, 2007, **398**, 33–37.

41 A. Orendorz, A. Brodyanski, J. Lösch, L. H. Bai, Z. H. Chen, Y. K. Le, C. Ziegler and H. Gnaser, *Surf. Sci.*, 2007, **601**, 4390–4394.

42 Q. Zhang, H. He, X. Huang, J. Yan, Y. Tang and H. Wang, *J. Chem. Eng.*, 2018, **332**, 57–65.

43 F.-F. Cao, X.-L. Wu, S. Xin, Y.-G. Guo and L.-J. Wan, *J. Phys. Chem. C*, 2010, **114**, 10308–10313.

44 H. He, Q. Gan, H. Wang, G.-L. Xu, X. Zhang, D. Huang, F. Fu, Y. Tang, K. Amine and M. Shao, *Nano Energy*, 2018, **44**, 217–227.

45 Z. Luo, S. Liu, Y. Cai, S. Li, A. Pan and S. Liang, *Energy Technol.*, 2018, **6**, 759–765.

46 O. Beyssac and M. Lazzeri, in *Raman spectroscopy applied to Earth sciences and cultural heritage*, ed. G. Ferraris, J. Dubessy, M.-C. Caumon and F. Rull, European Mineralogical Union, 2012, pp. 415–454.

47 A. Merlen, J. Buijnsters and C. Pardanaud, *Coatings*, 2017, **7**, 153.

48 M. N. Tahir, B. Oschmann, D. Buchholz, X. Dou, I. Lieberwirth, M. Panthöfer, W. Tremel, R. Zentel and S. Passerini, *Adv. Energy Mater.*, 2016, **6**, 1501489.